International Journal of Scientific Engineering and Research (IJSER)
ISSN (Online): 2347-3878
SJIF (2025): 8.036

# Catalytic Reduction of NO by CO over CuO/SBA-15: Reaction Engineering, Kinetics, and Application to Gasoline Engine Exhaust Treatment

**Bhavya Chopra[1], Rishabh Joshi[2]**

Department of Chemical Engineering

**Abstract:** ***This study investigates the catalytic reduction of NO by CO over CuO/SBA-15 as a cost-effective alternative to $NH_3$-SCR for gasoline exhaust treatment. A Mars–van Krevelen kinetic model is developed for the $Cu^{2+}/Cu^0$ redox cycle, and literature-derived kinetic parameters are employed to formulate a plug-flow reactor model. Temperature, CO:NO ratio, and gas-hourly-space-velocity effects are analysed for both intrinsic kinetics and effectiveness-factor-corrected behaviour. The catalyst exhibits a light-off temperature near 400–430°C and an optimal CO:NO ratio of approximately 1.5–2. Internal diffusion limitations are shown to be minimal for 50µm particles. The results indicate that CuO/SBA-15 is a promising supplementary $NO_x$ abatement technology for CO-rich and oxygen-lean gasoline exhaust streams.***

**Keywords:** CO-SCR; CuO/SBA-15; Mars–van Krevelen kinetics; $NO_x$ reduction; plug-flow reactor; gasoline exhaust treatment; internal diffusion; reaction engineering

## 1. Introduction

Nitrogen oxides ($NO_x$) emitted from gasoline (petrol) engine exhaust are a significant source of photochemical smog and contribute to secondary particulate formation and acid deposition. Three-pollutant control in gasoline exhaust – carbon monoxide (CO), unburned hydrocarbons (HC) and $NO_x$ – has historically been handled almost entirely by the three-way catalytic converter (TWC), a Pt/Pd/Rh washcoat operated under tightly controlled stoichiometric ($\lambda \approx 1$) conditions [7]. The TWC simultaneously oxidises CO and HC while reducing $NO_x$, but its $NO_x$-reduction efficiency collapses the moment the exhaust becomes oxygen-rich, which happens routinely during deceleration fuel cut-off, lean-burn or gasoline direct-injection (GDI) operating modes, and during the rich-to-lean transients used to regenerate lean $NO_x$ traps (LNTs).

The conventional fix for oxygen-rich $NO_x$ streams in diesel applications is urea/ammonia SCR ($NH_3$-SCR), but this brings its own penalties: a narrow effective temperature window (roughly 300–400°C), the risk of ammonia slip, reliance on a toxic $V_2O_5$-based catalyst that is itself poisoned by $SO_2$, and a separate reagent-dosing infrastructure that adds cost and packaging volume to a vehicle [7].

CO-SCR – the reduction of NO by CO according to

$$2NO + 2CO \longrightarrow N_2 + 2CO_2 \quad (1)$$

offers an internally consistent alternative: the reductant (CO) is already present in the exhaust stream, no external reagent is required, and a single catalyst bed removes both $NO_x$ and CO simultaneously. A stoichiometricallyoperated gasoline exhaust contains 0.1–2% CO, a few hundred to a few thousand ppm $NO_x$ (predominantly NO), and only a trace of $O_2$ when the air–fuel ratio is well controlled. Under lean-burn, GDI, or LNT-regeneration operation the $O_2$ content can rise to 1–3%, precisely the regime in which the Rh-based $NO_x$-reduction function of the TWC becomes ineffective.

CO-SCR over CuO/SBA-15 is not proposed here as a wholesale replacement for the TWC – under stoichiometric conditions the TWC remains the most mature and cost-effective solution. Rather, this chemistry is most relevant as (a) a secondary, underfloor $NO_x$-polishing stage active whenever CO is locally in excess of $O_2$ – e.g. during an LNT's rich purge – or (b) a base-metal $NO_x$ abatement stage for lean-burn/hybrid powertrains where frequent lean excursions reduce TWC effectiveness and a precious-metal-heavy secondary catalyst would be prohibitively expensive [5].

$NH_3$ vs CO as SCR reductants. $NH_3$-SCR ($4NH_3 + 4NO + O_2 \rightarrow 4N_2 + 6H_2O$) achieves > 90% $NO_x$ conversion and dominates industrial abatement from powerplant flue-gas to diesel trucks. Its strengths – maturity, selectivity, broad temperature window with Cu-zeolite catalysts – are offset by handling toxicity, ammonia slip requiring a downstream oxidation catalyst, sulfate fouling with $SO_2$-containing fuels, and the cost of a dedicated urea dosing infrastructure (urea freezes at ≈ −11°C). CO-SCR, by contrast, uses a reductant already present in the process gas – no separate reagent, simultaneous CO removal, no ammonia-slip pollutant – but is limited to $O_2$-lean streams (FCC off-gas, LNT purge gas) where direct CO oxidation does not outcompete the NO reduction pathway. The two chemistries are thus complementary, and the present work focuses on CO-SCR over CuO/SBA-15, a catalyst studied kinetically by Patel et al. [1] and for which the reduction half-cycle has been independently characterised by Goldstein and Mitchell [2]

## 2. Methodology

### 2.1 Catalyst: CuO/SBA-15

Three catalyst families dominate the CO-SCR literature: noble-metal systems (Pt, Pd, Rh on $Al_2O_3$), ironoxide systems ($Fe_2O_3$/SBA-15), and copper-oxide systems (CuO/SBA-15). The selection made here is CuO on SBA-15 at a Cu loading of 8.67 wt% (catalyst "CatB" in Patel et al. [1]), for four

reasons: (i) cost – copper is orders of magnitude cheaper than platinumgroup metals; (ii) mechanistic clarity – the $Cu^{2+}/Cu^0$ redox couple follows a textbook MvK cycle with explicit Arrhenius parameters for the reduction half-cycle [2]; (iii) performance – across conditions reported by Oliveira et al. [3, 4], CuO/SBA-15 consistently outperforms $Fe_2O_3$/SBA-15, both at stoichiometric CO:NO and in the presence of $O_2$ (Figure 1); (iv) regenerability – CuO/SBA-15 retains activity after four oxidative regeneration cycles (550°C $O_2$ flush) [4].

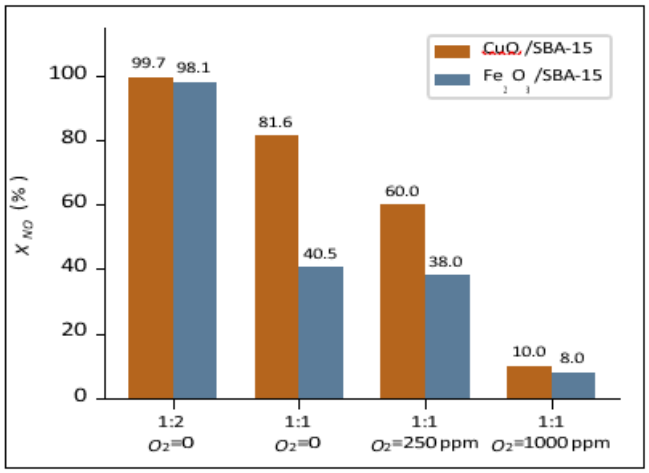


**Figure 1:** Literature comparison of CuO/SBA-15 and $Fe_2O_3$/SBA-15 (8.67 wt.% loading, $T$ = 500°C, GHSV= 48,000 $h^{-1}$) at NO:CO feed ratios of 1:2 and 1:1, with and without $O_2$. Data from Oliveira et al. [3, 4].

SBA-15 is an ordered, hexagonally-templated mesoporous silica with pore diameters of 6–9 nm and surface areas of 320–900 $m^2/g$ (vs. ∼1 $m^2/g$ for bulk CuO). The ordered, low-tortuosity ($\tau_p \approx 2.5$) pore network confines CuO crystallites to prevent sintering, gives a well-defined effective diffusivity (Section 2.5), and is hydrothermally stable above 600°C, suited to 400–550°C underfloor operation.

### 2.2 Reaction Chemistry and MvK Mechanism

The desired CO-SCR reaction is the two-for-two exchange of Equation 1. Two side reactions become relevant whenever CO is insufficient to reduce the nitrousoxide intermediate:

$$2NO + CO \longrightarrow N_2O + CO_2 \quad (2)$$
$$N_2O + CO \longrightarrow N_2 + CO_2 \quad (3)$$

$N_2O$ is a regulated greenhouse gas (∼298× $CO_2$ GWP over 100 years), so conditions that suppress Equation 2 or drive Equation 3 to completion are an important design objective.
Over CuO/SBA-15 the overall reaction proceeds through a two-step lattice-oxygen redox cycle (Figure 2): CO abstracts a lattice oxygen atom from CuO, reducing the copper site to $Cu^0$ and releasing $CO_2$ (Equation 4, $E_{red}$ = 20.0 kJ/mol); NO then re-oxidises the reduced site back to CuO, releasing $N_2$ (Equation 5, $E_{ox}$ = 132.9 kJ/mol):

$$CO + CuO \longrightarrow Cu^0 + CO_2 \quad (4)$$
$$NO + Cu \longrightarrow CuO + \frac{1}{2} N_2 \quad (5)$$

Let $\theta_{CuO}$ and $\theta_{Cu}0$ be the fractional coverages with $\theta_{CuO} + \theta_{Cu}0 = 1$. Under the pseudo-steady-state assumption the half-cycle rates are equal and both equal the overall rate $r$: $r = k_{red}P_{CO}\theta_{CuO} = k_{ox}P_{NO}\theta_{Cu}0$. Solving and substituting into the site balance gives the
MvK rate law,

$$r = \frac{k_{red}k_{ox}P_{CO}P_{NO}}{k_{red}P_{CO} + k_{ox}P_{NO}} \ [\text{molkg}{-}cat1\text{s}{-}1] \quad (6)$$

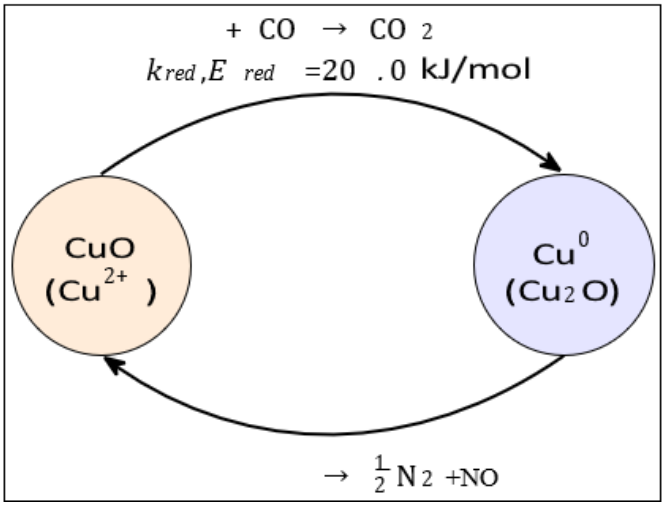


$k_{ox}, E_{ox}$ =132.9 kJ/mol

**Figure 2:** MvK redox cycle for CuO/SBA-15. The surface oscillates between an oxidised (CuO) and reduced ($Cu^0/Cu_2O$) state; CO supplies the reduction half-cycle and NO the (rate-limiting, below 453°C) oxidation halfcycle.

**Table 1:** MvK kinetic parameters for CuO/SBA-15.

| Param. | Value | Units | Source |
|---|---|---|---|
| $A_{red}$ | $4.6202 \times 10^{-4}$ | mol $kg_{cat}^{-1}s^{-1}Pa^{-1}$ | [1] |
| $E_{red}$ | 20,000 (20.0) | J/mol (kJ/mol) | [2] |
| $A_{ox}$ | $6.1076 \times 10^{4}$ | mol $kg_{cat}^{-1}s^{-1}Pa^{-1}$ | [1] |
| $E_{ox}$ | 132,933 (132.9) | J/mol (kJ/mol) | [1] |

with $P_{CO}$, $P_{NO}$ in Pa, $T$ in K. For an equimolar feed ($P_{CO} = P_{NO} = P_0(1 - X)$), Equation 6 collapses to a pseudo-first-order form with a harmonic-mean effective rate constant $k_{eff}$:

$$r = k_{eff}P_0(1 - X), \qquad k_{eff} = \frac{k_{red}k_{ox}}{k_{red} + k_{ox}} \quad (7)$$

### 2.3 Kinetic Parameters

No single publication reports a complete MvK parameter set ($A_{red}$, $E_{red}$, $A_{ox}$, $E_{ox}$) for CuO/SBA-15. The set used here (Table 1) was assembled from two complementary sources. $E_{red}$ = 20.0 kJ/mol is taken directly from the thermogravimetric study of Goldstein and Mitchell [2], who measured the CuO+CO→Cu+$CO_2$ step in isolation under confirmed kinetically-controlled conditions (particles < 125$\mu$m). The remaining parameters ($A_{red}$, $A_{ox}$, $E_{ox}$) were fitted so Equation 6 reproduces the conversion–temperature behaviour reported by Patel et al. [1] for Cat-B (8.67 wt% Cu/SBA-15, 500 ppm NO and CO in He, GHSV= 48,000 $h^{-1}$).

The resulting rate constants,

$$k_{red}(T) = 4.6202{\times}10^{-4} \exp\left(\frac{-20000}{8.314T}\right) \quad (8)$$

$$k_{ox}(T) = 6.1076{\times}10^{4} \exp\left(\frac{-132933}{8.314T}\right) \quad (9)$$

are plotted in Figure 3. Because $E_{ox} \gg E_{red}$, $k_{ox}$ rises far more steeply with $T$. Below the crossover at

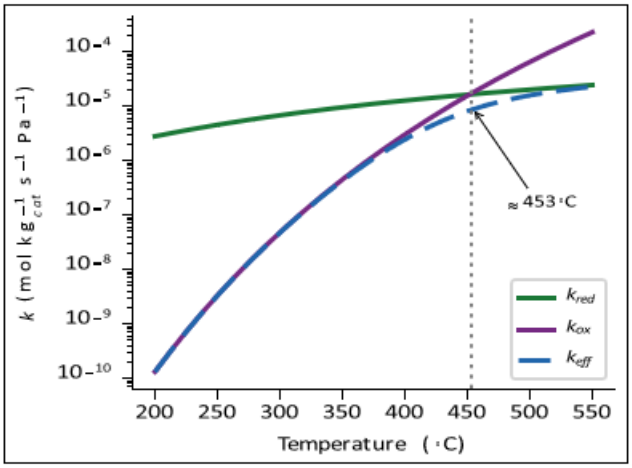


**Figure 3:** MvK rate constants $k_{red}$, $k_{ox}$ and harmonicmean $k_{eff}$ vs. temperature. The crossover at ≈ 453°C marks the change in rate-limiting step.

≈ 453°C, $k_{ox} < k_{red}$ and NO-dissociation is ratelimiting; above ≈ 453°C the surface is predominantly oxidised, waiting for CO.

### 2.4 PFR Reactor Model and Governing Equations

A steady-state mole balance for NO over a differential catalyst mass $dW$ of an ideal plug-flow reactor gives

$$F_{NO,0}\frac{dX}{dW} = r(T, P_{CO}, P_{NO}) \tag{10}$$

under the following standard PFR assumptions: (i) steady state; (ii) ideal plug flow – no axial dispersion or radial gradients; (iii) each sweep point is isothermal; (iv) ideal-gas behaviour; (v) negligible pressure drop and constant total molar flow, justified because NO and CO are present only at ppm–percent levels in a He balance, so the mole-change of Equation 1 (4 mol → 3 mol) alters total flow by < 0.01%.

General (non-equimolar) form. Substituting Equation 6 with $P_{NO} = P_0(1-X)$, $P_{CO} = P_0(R-X)$ for feed ratio $R$ =CO:NO:

$$F_{NO,0}\frac{dX}{dW} = \frac{k_{red}k_{ox}P_0^2(R-X)(1-X)}{k_{red}P_0(R-X) + k_{ox}P_0(1-X)} \quad ($$

For $R \neq 1$ this has no closed form and is integrated numerically (ratio sweep, Figure 6).

Equimolar specialization ($R = 1$). Equation 11 reduces to the pseudo-first-order form $F_{NO,0}dX/dW = k_{eff}P_0(1 - X)$, which integrates directly to

$$X_{NO} = 1 - \exp\left(-\frac{k_{eff}P_0W}{F_{NO,0}}\right) \tag{12}$$

used for the temperature and GHSV sweeps.

Effectiveness-factor-corrected form. When internal diffusion is non-negligible (Section 2.5), the intrinsic rate is scaled uniformly by $\eta(T)$:

$$F_{NO,0}\frac{dX}{dW} = \eta(T)\, r(T, P_{CO}, P_{NO}) \tag{13}$$

which for the equimolar case gives $X_{NO} = 1 - \exp(-\eta(T)k_{eff}(T)P_0W/F_{NO,0})$ – the $\eta$-corrected curves of the Results & Discussion.

### 2.5 Internal Mass-Transfer Analysis

The kinetic parameters of Table 1 are meaningful only if the data they were extracted from were kinetically (not diffusion) controlled. This is assessed using the Thiele modulus $\Phi_s$ and effectiveness factor $\eta(T)$. For a sphere $R_p = 50\mu$m (the fine SBA-15 powder of [1]), the Knudsen diffusivity is $D_K = \frac{d_{pore}}{3}\sqrt{\frac{8RT}{\pi M_{NO}}}$ ($d_{pore} = 6\times10^{-9}$ m) and $D_e = (\varepsilon_p/\tau_p)D_K$ ($\varepsilon_p = 0.569$, $\tau_p = 2.5$).

The Thiele modulus and effectiveness factor are

$$\Phi_s = R_p\sqrt{\frac{k_v\rho_c}{D_e}}, \quad k_v = k_{eff}RT, \quad \rho_c = 948 \text{ kg/m}^3 \tag{14}$$

$$\eta(T) = \frac{3}{\Phi_s}\left(\frac{1}{\tanh\Phi_s} - \frac{1}{\Phi_s}\right) \tag{15}$$

$\eta(T)$ is the fractional effectiveness of the catalyst particle: $\eta = 1$ means the rate is fully kinetically controlled; $\eta < 1$ means internal diffusion is suppressing it. $\eta(T)$ is plotted in Figure 4 and tabulated at key temperatures in Table 2.

### 2.6 Aspen HYSYS Simulation

The base case was implemented as an Aspen HYSYS flowsheet to generate parametric sweeps using the Databook Case Study tool, for both the intrinsic and $\eta$-corrected design equations.

Components and fluid package. NO, CO, $N_2$, $CO_2$, $N_2O$ and He (the inert balance gas). Peng–Robinson was selected as the fluid package for its better handling of the weakly polar NO and CO molecules in a dilute He carrier. Reactor block. An RPlug reactor was sized from the base case: $W_{cat} = 1\times10^{-4}$ kg catalyst ($\rho_c = 948$ kg/m$^3$) occupies a bed volume $V_{bed} \approx 0.105$ cm$^3$; for a 4 mm-ID tube this is a bed length of ≈ 8.4 mm with bed voidage $\varepsilon_b = 0.4$. Feed: $T = 400$°C, $P = 1$ atm, total molar flow $F_{total} = 5.45 \times 10^{-5}$ mol/s (≈ 73 mL/min at STP), matching the 80 mL/min of Patel et al. [1].

Implementing the MvK rate law (Equations 10– 13). HYSYS's native "Kinetic" reaction type assumes one Arrhenius pair per power-law rate. Equation 6 is instead a sum-of-resistances expression in two independently-Arrhenius constants and cannot be collapsed into this form without error: a single bestfit lumped Arrhenius pair for $k_{eff}(T)$ over 350–550°C ($A_{eff} = 7.81$, $E_{eff} = 84.7$ kJ/mol) is in error by −26% at 450°C and +46% at 550°C due to the curvature in Figure 3. The MvK rate was therefore evaluated exactly via a Spreadsheet operation attached to the reactor: at each cell the spreadsheet reads local $T$, $P_{NO}$, $P_{CO}$ from the RPlug profile, evaluates $k_{red}(T)$, $k_{ox}(T)$ and $\eta(T)$ (Equation 15), computes $r$ from Equation 6 and $r_{eff} = \eta(T)r$ from Equation 13, and returns either value to a zeroorder "User" kinetic reaction ($A = 1$, $E_a = 0$) – a toggle selects $\eta = 1$ (intrinsic) or $\eta = \eta(T)$ (corrected) for each Case Study run.

Validation. Substituting $k_{eff}(673\text{ K}) = 2.41 \times 10^{-6}$ molkg$^{-1}$s$^{-1}$Pa$^{-1}$ into Equation 12: $X_{NO} = 36.0\%$ at

$T$ = 400°C ($P_{NO}$ = $P_{CO}$ = 50.66 Pa, $W_{cat}$ = 1×10$^{-4}$ kg, $F_{NO,0}$ = 2.727×10$^{-8}$ mol/s), matching the experimental value of Patel et al. [1]. This confirmed base case is the basis for all sweeps below.

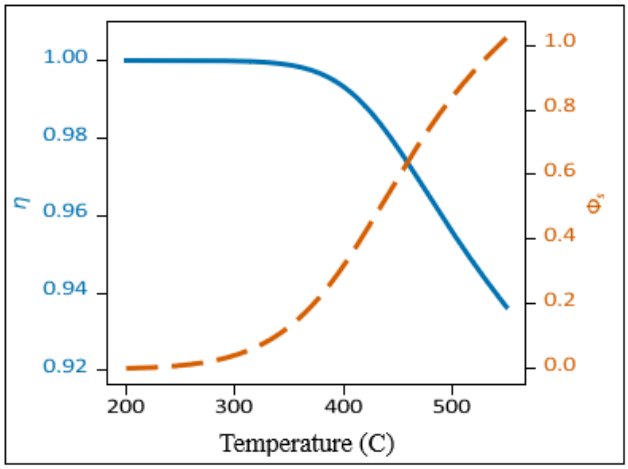


**Figure 4:** Thiele modulus $\Phi_s$ (right axis) and effectiveness factor $\eta(T)$ (left axis, Equation 15) for a 50 $\mu$m CuO/SBA-15 particle, 200–550°C.

## 3. Results & Discussion

### 3.1 Effectiveness Factor vs. Temperature

Figure 4 shows $\Phi_s$ and $\eta(T)$ over 200–550°C. Below ~350°C, $\Phi_s \to 0$ and $\eta \to 1$ – the catalyst is essentially intrinsic throughout the low-temperature half of the sweep. At the validation point (400°C), $\Phi_s$ = 0.32 and $\eta$ = 0.993, confirming the literature data and Table 1 are intrinsic ($C_{WP} \ll 1$). Above ≈ 450°C, $\eta$ falls measurably – 0.978 at 450°C, 0.956 at 500°C, 0.937 at 550°C. For 50 $\mu$m particles this is a < 7% correction even at 550°C, but it scales with $R_p^2$ – for larger pellets or thicker washcoats this correction would need re-evaluation at every operating point.

### 3.2 Temperature Sweep: Light-off Behaviour

Figure 5 shows $X_{NO}$ vs. temperature over 200–550°C at CO:NO=1:1 (Equation 12 and its $\eta$-corrected equivalent). Both curves exhibit the classic S-shaped "light-off" profile: negligible below 300°C ($k_{ox} \ll k_{red}$, NO-dissociation essentially frozen), rising steeply through 350–450°C as $k_{ox}$ catches up with $k_{red}$, and approaching complete conversion above 500°C. The inflection – around 400–430°C – is the practically important light-off temperature for this catalyst.

Table 2 gives the two curves at five temperatures. The $\eta$-correction is small everywhere: at 400°C, $X_{NO}$ falls from 36.03% ($\eta$ = 1) to 35.84% ($\eta(T)$), and the largest absolute deviation across the full sweep is only ≈ 0.8 percentage points near 450–500°C (where $\Phi_s$ is largest). Both curves pass through the Patel datum (36.0% at 400°C). This confirms that, for 50 $\mu$m particles, the intrinsic curve of Equation 12 is an adequate design tool across the full operating range, with the $\eta$-correction only becoming significant for larger pellets or thicker automotive washcoats.

### 3.3 CO:NO Ratio Sweep

Figure 6 shows $X_{NO}$ at 400°C as feed CO:NO is varied 0.25–4 (Equation 11 integrated numerically), again for $\eta$ = 1 and $\eta$ = $\eta$(400°C) = 0.9933. Because this sweep is isothermal, $\eta$ takes the single value 0.9933 for every point,

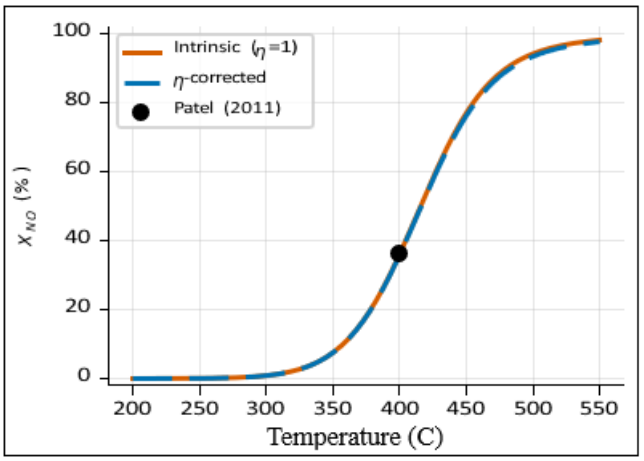


**Figure 5:** Temperature sweep, CO:NO=1:1, GHSV= 48,000 h$^{-1}$: intrinsic ($\eta$ = 1) vs. $\eta(T)$-corrected, with the validation point from Patel et al. [1].

**Table 2:** Temperature sweep: intrinsic vs. $\eta$-corrected $XNO$

| $T$ (°C) | $\eta(T)$ | $X_{NO}$, $\eta$=1 | $X_{NO}$, $\eta(T)$ | Δ (pp) |
|---|---|---|---|---|
| 350 | 0.999 | 7.51% | 7.50% | 0.01 |
| 400 | 0.993 | 36.03% | 35.84% | 0.19 |
| 450 | 0.978 | 77.16% | 76.39% | 0.77 |
| 500 | 0.956 | 94.44% | 93.69% | 0.75 |
| 550 | 0.937 | 98.43% | 97.96% | 0.47 |

giving a near-constant ≈ 0.2 percentage-point downward shift between the two curves.

Below the stoichiometric ratio of 1, conversion is reductant-limited and falls sharply – at CO:NO= 0.5, $X_{NO}$ ≈ 29%. Above ~1.5–2, both curves flatten: at 400°C, the NO-dissociation step is already the bottleneck (Section 2.3), so extra CO cannot accelerate a step it is not part of. This identifies an economically optimal CO:NO of ~1.5–2, beyond which excess CO is unconverted reductant.

### 3.4 GHSV Sweep

Figure 7 shows $X_{NO}$ at 400°C, CO:NO=1:1, as GHSV is varied 8,000–100,000 h$^{-1}$ (Equation 12). As with the ratio sweep, $T$ is fixed so $\eta$ is constant, giving a near-uniform ≈ 0.2 percentage-point downward shift: from 83.26%→83.05% at GHSV= 12,000 h$^{-1}$ to 20.02%→19.90% at GHSV= 96,000 h$^{-1}$. Since $F_{NO,0}$ ∝GHSV, conversion falls monotonically: a smaller catalyst bed (higher GHSV for fixed flow) sacrifices conversion. Figure 7 is the primary design chart for sizing a bed to a target $X_{NO}$ at a given exhaust flow rate; the $\eta$-correction shifts the required bed mass by < 1% for 50 $\mu$m particles.

### 3.5 Sensitivity to Oxygen

The kinetic model has no explicit $O_2$ term, but the literature data of Figure 1 make the effect unmistakable: at $T$ = 500°C, CO:NO=1:1, $X_{NO}$ falls from 81.6% (no $O_2$) to 60.0% (250 ppm $O_2$) to 10.0% (1000 ppm $O_2$). $O_2$ competes directly with NO

for reduced $Cu^0$ sites and consumes CO via $2CO + O_2 \rightarrow 2CO_2$, removing reduc-

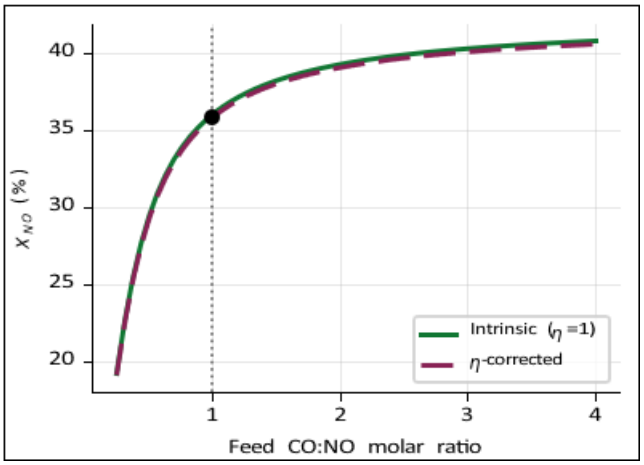


**Figure 6:** CO:NO feed-ratio sweep at $T = 400$°C: intrinsic ($\eta = 1$) vs. $\eta$-corrected ($\eta = 0.9933$, constant since $T$ is fixed). Black marker: base case (CO:NO=1).

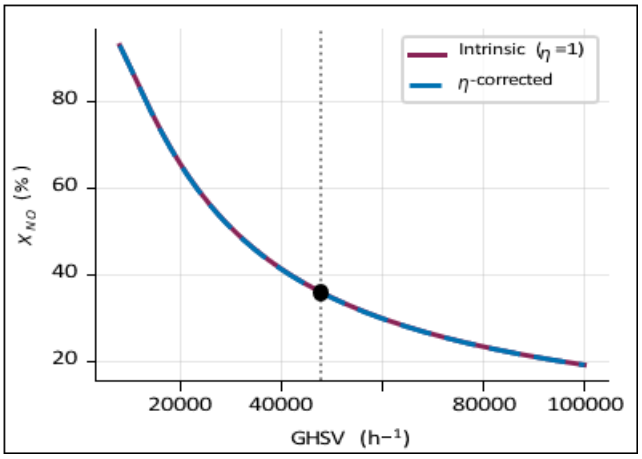


**Figure 7:** GHSV sweep at $T = 400$°C, CO:NO=1:1: intrinsic ($\eta = 1$) vs. $\eta$-corrected ($\eta = 0.9933$). Black marker: base case (GHSV= 48,000 $h^{-1}$).

tant before the MvK cycle completes. As a rule of thumb, the cycle is severely disrupted once $O_2$:CO exceeds ∼0.5 – the most important constraint on where this chemistry can be deployed in a real exhaust system.

### 3.6 Heat of Reaction and Industrial Utilisation

Using standard enthalpies of formation, the enthalpies of the CO-SCR reactions (Table 3) are all strongly exothermic; the main reaction releases ≈ 373 kJ per mole of NO reduced – comparable to CO oxidation ($\Delta H = -283$ kJ/mol CO).

For an adiabatic bed, $\Delta T_{ad} \approx y_{NO,0} X_{NO} |\Delta H_{rxn}| / C_{p,mix}$. At automotive concentrations ($y_{NO,0}$ = 500 ppm, $C_{p,mix} \approx 33$ $Jmol^{-1}K^{-1}$), even complete conversion gives $\Delta T_{ad} \approx 5.7$ K – negligible. CO-SCR itself is not a significant automotive heat source; the dominant exotherm in a real TWC is CO/HC oxidation by $O_2$. However, at industrial $NO_x$/CO loadings (FCC regenerator, sinter plant, nonferrous smelter) the same reaction sees adiabatic rises of tens to over a hundred kelvin, exploited industrially as follows:

**Table 3:** Enthalpy of the CO-SCR reactions.

| Reaction | $\Delta H_{rxn}$ |
|---|---|
| $2NO+2CO \rightarrow N_2+2CO_2$ | −746.5 kJ (−373.3/mol NO) |
| $2NO+CO \rightarrow N_2O+CO_2$ | −381.5 kJ |
| $N_2O+CO \rightarrow N_2+CO_2$ | −365.1 kJ |

Light-off acceleration and autothermal operation. The reaction's own heat sustains bed temperature once light-off is reached, reducing external heating needs – the "selfheating" mechanism exploited in autothermal reactor design.

Heat recovery and integration. In large stationary units, the temperature rise is recovered via gas–gas exchangers to preheat feed, or waste-heat boilers for steam. In automotive contexts, the broader practice of exhaust heat recovery (thermoelectric generators, oil/coolant warming at cold start) captures part of the overall exhaust enthalpy, of which the CO-SCR exotherm is one minor contributor.

Thermal management and staged reactors. Where the adiabatic rise is large, a single bed risks an excessive outlet temperature and hot spots exceeding the support's safe limit. The standard mitigation is a multi-bed reactor with intercooling between stages – Figure 5 is the tool used to choose the inlet temperature and bed length of each stage.

### 3.7 Application in Petrol Exhaust Systems

Temperature window. Figure 5 shows useful conversion (> 10%) from ∼330°C and > 75% by 450°C, spanning the bulk of an underfloor catalyst's range during warmed-up driving (300–500°C), and broader than $NH_3$SCR's 300–400°C window. The catalyst is inactive below ∼250°C at cold start.
Reductant availability. In a well-tuned stoichiometric engine the TWC consumes essentially all CO and $O_2$, leaving little for a downstream CO-SCR stage. This chemistry is best matched to (i) LNT rich-purge pulses – deliberately CO/$H_2$-rich and $O_2$-lean, exactly where Figure 1 shows CuO/SBA-15 performing best (99.7% at NO:CO=1:2) – or (ii) lean-burn/GDI engines with controlled excess CO and limited $O_2$.
Packaging. Table 1's parameters come from a packed bed of fine (< 125$\mu$m) powder; automotive converters are monolithic honeycombs with thin (10–50 $\mu$m) washcoats. Equation 6 translates directly (rate per unit mass unchanged), but the packed-bed PFR model would need re-casting to a monolith-channel model – with $\Phi_s$ even smaller and $\eta$ even closer to unity than Table 2 (a thin washcoat is, if anything, less diffusion-limited than the 50 $\mu$m particles studied here).

### 3.8. Benefits and Disadvantages of CuO/SBA-15 COSCR

**Benefits**
Simultaneous NO and CO removal in one bed, no external reductant infrastructure or reagent supply chain.

Base-metal (Cu) active phase: far cheaper than Pt/Pd/Rh; avoids $V_2O_5$/$NH_3$-SCR toxicity and $SO_2$poisoning penalties.

Broad effective temperature window (light-off ∼330°C, > 75% by 450°C), wider than $NH_3$-SCR.

Mesoporous SBA-15 gives high surface area, defined pore architecture, and good hydrothermal stability with demonstrated multi-cycle regenerability.

Well-understood MvK redox cycle: the rate-limiting step (dominant design lever) is identifiable at any $T$, and the PFR model (Section 2.4) provides clear reactor sizing equations.

The CO-SCR exotherm contributes to self-sustaining (autothermal) operation once light-off is reached.

**Disadvantages**

Severe $O_2$ inhibition: $X_{NO}$ falls from > 80% to ~10% as $O_2$ rises 0–1000 ppm, restricting deployment to CO-rich/$O_2$-lean exhaust (e.g. LNT purge) rather than the bulk stream.

Possible $N_2O$ formation (Equation 2), itself a greenhouse gas, requiring sufficient CO and residence time via Equation 3.

High $E_{ox}$ = 132.9 kJ/mol limits low-temperature (cold-start) activity intrinsically.

Internal mass-transfer resistance becomes measurable above ~450°C for larger particles/washcoats (Table 2).

Long-term durability (steam, sulfur, thermal cycling) is less documented than commercial TWC formulations.

Requires reliable CO at the inlet; in a well-tuned stoichiometric engine CO is largely consumed upstream, leaving little reductant unless specifically positioned.

### 3.9. Further Research Directions

The validated baseline established here (MvK kinetics, PFR model, intrinsic/$\eta$-corrected sweeps) motivates the following extensions:

Fitted $O_2$-inhibition term. Regress a Langmuir-type term $K_{O2}P_{O2}$ into the denominator of Equation 6, alongside a non-selective $2CO + O_2 \rightarrow 2CO_2$ pathway. This is the single most important remaining step, directly determining the feasible operating window.

Side-reaction ($N_2O$) kinetics. Fitting rate parameters for Equations 2–3 would let the sweeps report $N_2O$ selectivity alongside $X_{NO}$, critical for regulatory compliance.

Non-isothermal PFR. Couple Equation 10 to an energy balance using Table 3 to predict axial temperature profiles and hot-spots – most relevant at the higher $NO_x$/CO loadings of industrial applications.

Monolith/washcoat geometry. Re-cast the packed-bed PFR as a monolith-channel model with washcoat scale diffusion, re-evaluating $\eta$ at the much smaller washcoat thickness.

Broader experimental validation. The model is validated against a single datum. Digitising Patel's full conversion–temperature curve and the $O_2$-sweep data of Figure 1 would enable direct multi-point validation.

Catalyst durability and poisoning. Long-term $SO_2$ exposure, steam aging, and Cu sintering/redispersion under realistic thermal cycling remain undocumented for this catalyst and are essential for commercialisation.

Combined operating map. Merge the temperature, CO:NO, GHSV and $O_2$ sweeps into one operating map for sizing a bed to a target $X_{NO}$ across a full drive cycle.

CFD/2-D modelling. For larger-diameter industrial reactors, relax the plug-flow assumption with a 2-D or CFD model that captures radial concentration/temperature gradients.

## Conclusion

This study presents a comprehensive reaction-engineering analysis of NO reduction by CO over CuO/SBA-15. The Mars–van Krevelen kinetic model, plug-flow reactor formulation, and effectiveness-factor analysis successfully describe catalyst behaviour across a range of operating conditions. The catalyst exhibits favourable activity at elevated temperatures, minimal diffusion limitations for small particles ($\eta \geq 0.99$ at 400°C), and an optimal CO:NO ratio near 1.5–2. Although oxygen sensitivity restricts operation to CO-rich and oxygen-lean environments, CuO/SBA-15 shows promise as a supplementary $NO_x$ abatement technology for lean-burn and GDI powertrains, particularly during LNT regeneration purge cycles where the feed is deliberately CO/$H_2$-rich and $O_2$-lean. Comparison with $NH_3$-SCR confirms the two approaches are complementary: $NH_3$-SCR is better suited to continuous, high-concentration $NO_x$ streams, while CO-SCR offers a reagent-free solution for intermittent, CO-rich operating windows. Future work should address $O_2$-inhibition kinetics, $N_2O$ side-reaction pathways, non-isothermal reactor modelling, and monolith-scale washcoat diffusion to complete the design framework for practical deployment.

## References

[1] Patel, A.; Thomas, R.E.; Rudolph, V.; Zhu, Z. Selective catalytic reduction of NO by CO over CuO supported on SBA-15: Effect of CuO loading on the activity of catalysts. Catal. Today 166 (2011) 188–193.
[2] Goldstein, E.A.; Mitchell, R.E. Chemical kinetics of copper oxide reduction with carbon monoxide. Proc. Combust. Inst. 33 (2011) 2803–2810.
[3] de Oliveira, A.C.; da Silva Rocha, K.A.; de Sousa, B.V.; Filho, C.R. Optimizing reaction conditions for selective catalytic reduction of NO by CO over supported SBA-15 catalysts. Environ. Sci. Pollut. Res. 27 (2020) 30649–30660.
[4] de Oliveira, A.C.; Rodrigues, M.V.; Rossa, V.; Garcia, M.A.S. Selective catalytic reduction of $NO_x$ by CO over Cu(Fe)/SBA15 catalysts: Effects of metal loading on catalytic activity. Catalysts 13 (2023) 527.
[5] Granger, P.; Lecomte, J.J.; Dathy, C.; Leclercq, L.; Leclercq, G. A comparative kinetic study of the NO + CO reaction over Pt, Rh and Pd catalysts. Top. Catal. 39 (2006) 161–170.
[6] Wilkinson, S.K.; van de Water, L.G.A.; Miller, B.; Simmons, M.J.H.; Stitt, E.H.; Watson, M.J. Understanding the generation of methanol synthesis and water gas shift activity over copper-based catalysts. Top. Catal. 63 (2020) 816–829.

[7] Heck, R.M.; Farrauto, R.J.; Gulati, S.T. Catalytic Air Pollution Control: Commercial Technology, 3rd ed. Wiley: New York, 2009.
[8] NIST Chemistry WebBook. National Institute of Standards and Technology, 2023. Standard enthalpies of formation: CO, NO, $CO_2$, $N_2O$. https://webbook.nist.gov.